Statistical properties of two-dimensional elastic turbulence

Himani Garg ⬤, Enrico Calzavarini ⬤, and Stefano Berti ⬤

Université de Lille, ULR 7512–Unité de Mécanique de Lille Joseph Boussinesq (UML), F-59000 Lille, France

We numerically investigate the spatial and temporal statistical properties of a dilute polymer solution in the elastic turbulence regime, i.e., in the chaotic flow state occurring at vanishing Reynolds and high Weissenberg numbers. We aim at elucidating the relations between measurements of flow properties performed in the spatial domain with the ones taken in the temporal domain, which is a key point for the interpretation of experimental results on elastic turbulence and to discuss the validity of Taylor's hypothesis. To this end, we carry out extensive direct numerical simulations of the two-dimensional Kolmogorov flow of an Oldroyd-B viscoelastic fluid. Static pointlike numerical probes are placed at different locations in the flow, particularly at the extrema of mean flow amplitude. The results in the fully developed elastic turbulence regime reveal large velocity fluctuations, as compared to the mean flow, leading to a partial breakdown of Taylor's frozen-field hypothesis. While second-order statistics, probed by spectra and structure functions, display consistent scaling behaviors in the spatial and temporal domains, the third-order statistics highlight robust differences. In particular the temporal analysis fails to capture the skewness of streamwise longitudinal velocity increments. Finally, we assess both the degree of statistical inhomogeneity and isotropy of the flow turbulent fluctuations as a function of scale. While the system is only weakly nonhomogenous in the cross-stream direction, it is found to be highly anisotropic at all scales.

I. INTRODUCTION

Viscoelastic fluids are known to be characterized by non-Newtonian behavior under appropriate conditions. In particular, dilute polymer solutions may display non-negligible elastic forces when the suspended polymeric chains occur to be sufficiently stretched by fluid velocity gradients. Remarkably, when the elasticity of the solution overcomes a critical value, such forces can trigger instabilities that can eventually lead to irregular turbulent-like flow, even in the absence of fluid inertia, namely in the limit of vanishing Reynolds number (Re). The latter dynamical regime is known as elastic turbulence (ET) [1] and it has been experimentally observed in different flow configurations [1–6]. The emergence of this regime is characterized by the fast growth of the (largest) Lyapunov exponent of the flow as the polymer elasticity exceeds a system-dependent critical value [7,8]. Besides, the kinetic-energy spatial and temporal spectra have a power-law behavior of exponent larger than 3, in absolute value, which indicates the presence of a multiplicity of active scales in the flow. The spatial spectrum, however, is steeper than for Newtonian (three-dimensional) turbulence, i.e., velocity fluctuations are concentrated at small wavenumbers; hence the velocity field is smooth in space [1,6,9].

Based on its similarity with turbulent fluid motion, elastic turbulence has been proposed as an efficient system to enhance mixing in low-Reynolds-number flows [2]. Moreover, it has been shown that it can increase heat transfer [10,11] and promote emulsification [12]. Recently, it has also been argued that elastic turbulence flows play a significant role in the increased oil displacement obtained in industrial processes

employing dilute polymer solutions to flood porous reservoir rocks [13].

A compact and effective review of the main theoretical results on ET [14] can be found in [4], where several aspects of the agreement between the theory and experiments have been studied (see also Refs. [6,9]). We have shown in previous work [8,15,16] that the main features of elastic turbulence can be numerically reproduced using a minimal flow model of a highly elastic polymer solution at low Re. Specifically, we considered the dynamics of Oldroyd-B model in a two-dimensional (2D) nonhomogeneous, periodic, Kolmogorov flow setup.

Here we perform a more thorough numerical study of the statistical properties of ET in the same system. We focus on single- and multipoint statistics in both the temporal and spatial domains. We aim at elucidating the relations between measurements of flow properties performed in the spatial domain with the ones taken in the temporal domain, which is a key point for the interpretation of experimental results on elastic turbulence [4,6,17]. On the other hand, we aim to quantify the homogeneity and isotropy properties of the velocity fluctuations occurring in our flow. In particular, we examine the probability distribution function (PDF) of the fluctuating velocity and of its derivatives, as well as the velocity power spectra, and the structure functions of velocity increments, in both the temporal and the spatial domain, at different flow locations. We further address the validity of Taylor's frozen turbulence hypothesis as done in experiments [18], in our numerical ET flows.

This article is organized as follows. The model used to describe the dynamics of the viscoelastic fluid is introduced in
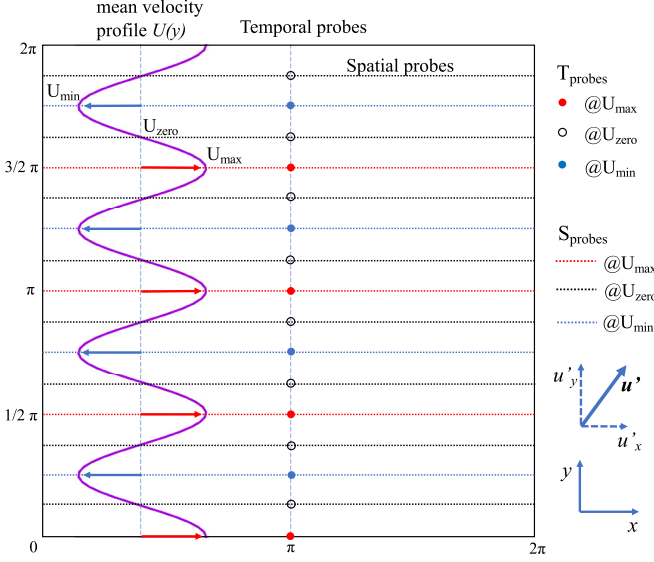
FIG. 1. Positions of the different probes in the Kolmogorov flow setup. The large square box represents the spatial domain with size $[0, 2\pi] \times [0, 2\pi]$, while the solid violet line represents the mean velocity profile $U(y) = U \cos(ky)$, which has local maxima, minima, and nodes denoted U_{max}, U_{min}, and U_{zero}. The positions of the point-like temporal probes T_{probes} are denoted by colored bullet symbols, while the positions of local spatial probes are indicated by the horizontal dashed lines.

Sec. II. In Sec. III, after briefly illustrating the main properties of the flow fields, we present the results about single- and two-point statistics both in the temporal and in the spatial domain. Conclusions are presented in Sec. IV.

II. MODEL DYNAMICS AND SIMULATIONS

A. The 2D Kolmogorov flow for a viscoelastic fluid

We consider the dynamics of a dilute polymer solution as described by the Oldroyd-B model [19]:

$$\partial_t \boldsymbol{u} + (\boldsymbol{u} \cdot \nabla)\boldsymbol{u} = -\frac{\nabla p}{\rho_f} + \nu_s \Delta \boldsymbol{u} + \frac{2\eta\nu_s}{\tau}\nabla \cdot \boldsymbol{\sigma} + \boldsymbol{f}, \quad (1)$$

$$\partial_t \boldsymbol{\sigma} + (\boldsymbol{u} \cdot \nabla)\boldsymbol{\sigma} = (\nabla \boldsymbol{u})^T \cdot \boldsymbol{\sigma} + \boldsymbol{\sigma} \cdot (\nabla \boldsymbol{u}) - 2\frac{\boldsymbol{\sigma} - \mathbf{1}}{\tau}. \quad (2)$$

In the above equations $\boldsymbol{u} = (u_x, u_y)$ is the incompressible velocity field, the symmetric positive definite matrix $\boldsymbol{\sigma}$ represents the normalized conformation tensor of polymer molecules (normalized with the squared gyration radius) and $\mathbf{1}$ is the unit tensor corresponding to the equilibrium configuration of polymers attained in the absence of flow ($\boldsymbol{u} = 0$). The trace tr($\boldsymbol{\sigma}$) gives the local polymer mean-squared elongation while τ represents the largest typical polymer relaxation time. The fluid density is denoted ρ_f and the total viscosity of the solution is $\nu = \nu_s(1 + \eta)$, with ν_s the kinematic viscosity of the solvent and η the zero-shear contribution of polymers (which is proportional to polymer concentration). The extra stress term $\frac{2\eta\nu_s}{\tau}\nabla \cdot \boldsymbol{\sigma}$ accounts for elastic forces providing a feedback mechanism on the flow [14,20].

In this study we are interested in a fluid velocity field characterized by a nonhomogeneous mean flow and turbulent fluctuations generated by elastic stresses only. This is provided by the 2D periodic Kolmogorov flow. In the context of viscoelastic fluids, this flow has been previously adopted in Refs. [8,15,21] in order to provide a simple and effective model able to reproduce the basic phenomenology of elastic turbulence. Using the Kolmogorov forcing $\boldsymbol{f} = (F \cos(ky), 0)$ in Eq. (1), one has a laminar fixed point corresponding to the velocity field $\boldsymbol{u}^{(0)} = (U_0 \cos(ky), 0)$ and the conformation tensor components $\sigma_{11}^{(0)} = 1 + \frac{\tau^2 k^2 U_0^2}{2} \sin^2(ky)$, $\sigma_{12}^{(0)} = \sigma_{21}^{(0)} = -\frac{\tau k U_0}{2} \sin(ky)$, $\sigma_{22}^{(0)} = 1$, with $F = \nu k^2 U_0$ [22]. From these expressions, the characteristic length and velocity scales $L = 1/k$ and U_0, respectively, can be identified. As previously documented, the laminar flow becomes unstable [22] for sufficiently high values of elasticity, even in the absence of fluid inertia, and eventually displays features typical of turbulent flows [8,15,16,21]. In the elastic turbulence regime, the mean velocity and conformation tensor fields keep similar simple sinusoidal functional forms but with different amplitudes. Denoting $U(y) = L_0^{-1} \int_0^{L_0} u_x(x, y) \, dx$ the mean longitudinal velocity and U its amplitude, where L_0 is the domain size (along the x axis), we define the Reynolds number as Re $= UL/\nu$ and the Weissenberg number as Wi $= U\tau/L$.

B. Numerical methods

Equations (1) and (2) are integrated using a pseudo spectral method on a grid of side $L_0 = 2\pi$ with periodic boundary conditions at resolution 512^2. We verified that the simulation results are independent of the mesh size. Integration of viscoelastic models is limited by instabilities associated with the loss of positiveness of the conformation tensor [23]. These instabilities are particularly relevant at high Wi values and limit the possibility to numerically investigate the elastic turbulence regime by direct implementation of the equations of motion. For this reason we adopt an algorithm based on a Cholesky decomposition of the conformation matrix ensuring symmetry and positive definiteness [24,25]; to stabilize the code a small polymer diffusivity, corresponding to a Schmidt number Sc $\approx 10^3$, was also added. For Kolmogorov and similar external forces that mix strain and vorticity, the effect of artificial polymer diffusivity may be less dramatic than in purely elongational flows [26,27]. This approach allows us to reach sufficiently high elasticity; however, it imposes some limitations in terms of resolution and computational time. We fix Re $= 1$ (using the value of U_0 to obtain an *a priori* estimate of it), which is smaller than the critical value $\sqrt{2}$ of the Newtonian case [28], and we choose a value of Wi larger than the critical one $\text{Wi}_c \approx 10$ corresponding to the onset of purely elastic instabilities [15]. The other parameters of the viscoelastic dynamics are $U_0 = 4$, $L = 1/4$, $\nu_s = 0.769$, $\eta = 0.3$, and $\tau = 2.5$. The initial condition is obtained by adding a small random perturbation to the fixed point solution $\boldsymbol{u}^{(0)}, \boldsymbol{\sigma}^{(0)}$, and the system is evolved in time until a statistically steady state is reached. To accelerate the convergence, indeed quite slow, of the velocity statistics, the results are obtained by further averaging over an ensemble of five independent data sets, each of which was obtained from simulations begun with slightly different random initial conditions. In a recent work [16], we have already shown that the resulting dynamics are only quite weakly dependent on Wi in the fully
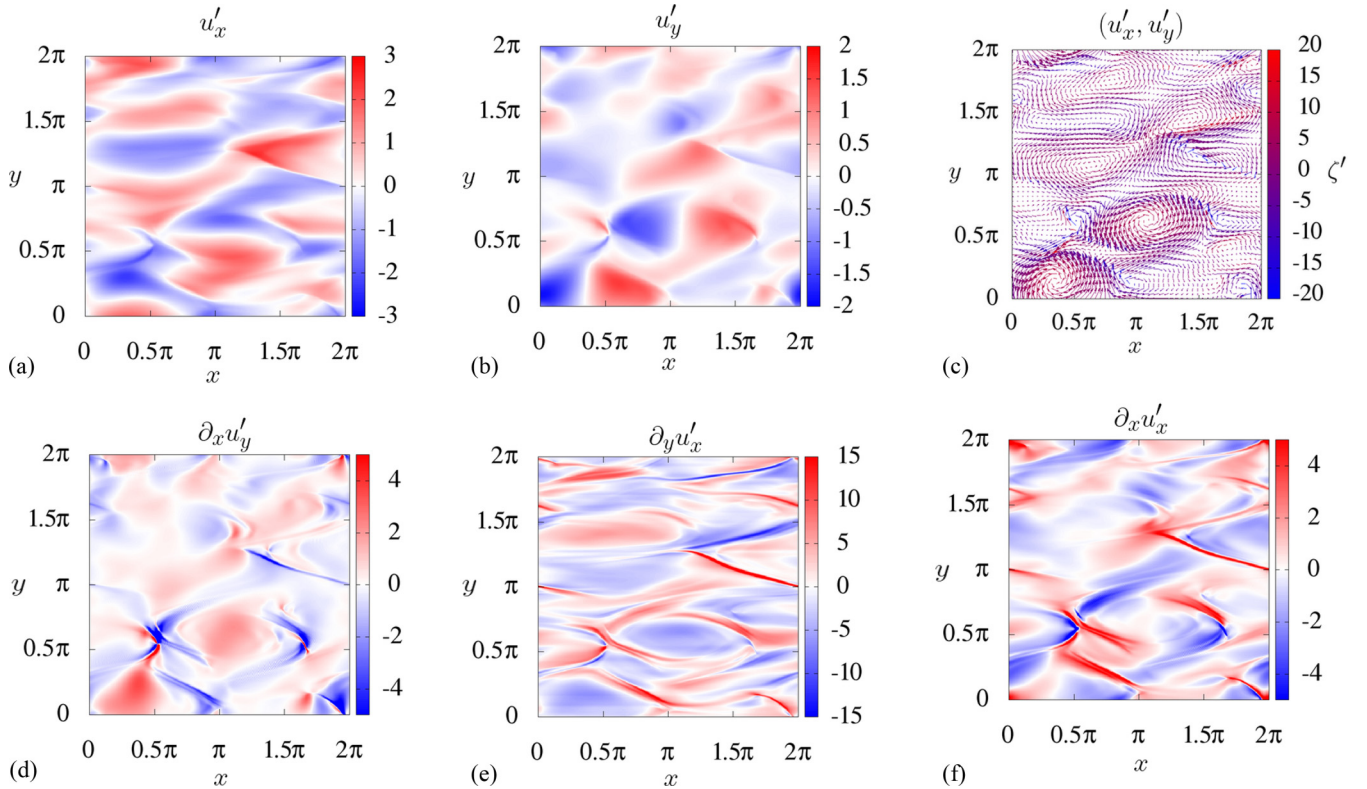
FIG. 2. Instantaneous snapshots of $u'_x(x, y)$ (a), $u'_y(x, y)$ (b), $\partial_x u'_y$ (d), $\partial_y u'_x$ (e), and $\partial_x u'_x$ (f). Panel (c) shows the vector-field representation of the fluctuating velocity $\boldsymbol{u}'$ at the same instant of time as the other panels; here the color codes the intensity of the fluctuating vorticity ζ'.

developed elastic turbulence regime. Hence, in the following we will only consider a single Weissenberg number, namely Wi = 24.9 [16].

In this study, we look at the flow in its statistically steady state from two different perspectives. The first is via spatial information obtained by instantaneous velocity fields stored during the simulations, the second is by analyzing time series taken at specific locations in the flow. While the first procedure is in principle preferable, as it may allow access to any relevant physical quantity, the second one is closer to the approach sometimes taken in experiments, in which the full dynamical field of interest is not always easily accessible (but note that, through the digital particle velocimetry technique, long time series of full spatial distributions of velocity were obtained for ET [4,9,18]). To obtain the time series for the temporal analysis, we place static pointlike temporal probes at different locations in the computational domain, in particular in the positions where the mean flow is maximum, minimum, and zero, denoted @$U_{\max}$, @$U_{\min}$, and @U_{zero} (as shown in Fig. 1). We will then compare the measurements from these two viewpoints in a systematic way, highlighting the limitations intrinsically connected to probelike single-point temporal data. In fact, the availability of these two different data sets is interesting to assess the validity of Taylor's hypothesis.

III. RESULTS

A. The fluctuating velocity field

To look at the peculiar statistical features of the ET flow, it is convenient to consider the fluctuating component of the

velocity field, defined as $\boldsymbol{u}'(x, y) = \boldsymbol{u}(x, y) - U \cos(ky)\hat{\boldsymbol{x}}$ (with $\hat{\boldsymbol{x}}$ the unit vector in the streamwise direction). Figure 2 displays an instantaneous snapshot of $\boldsymbol{u}'$ at Wi = 24.9. The figure shows separately the streamwise component u'_x [Fig. 2(a)], the cross-stream component u'_y [Fig. 2(b)], and the full vector field $\boldsymbol{u}'$ [Fig. 2(c)] colored according to the intensity of the instantaneous fluctuating vorticity field $\zeta' = \partial_x u'_y - \partial_y u'_x$. Altogether, such a visualization allows us to easily appreciate the presence of secondary vortical structures emerging on top of the unidirectional mean background flow. These vortices appear to be stretched along the y direction, probably as an effect of the mean flow. Their width along the x direction carries the imprint of the characteristic length scale of the forcing. Overall, the secondary flow structures are observed to be organized in alternating stripes of counter-rotating eddies. Figures 2(d)–2(f) in the same figure show the components of the velocity gradient tensor at the same instant of time. Note that only three independent components exist here due to incompressibility ($\partial_y u'_y = -\partial_x u'_x$). The spatial structure of the gradient fields reveals the existence of thin boundary regions between adjacent vortices. An example of the data obtained from pointlike probes is provided in Fig. 3. Specifically, here Figs. 3(a) and 3(b) respectively show the time series of the fluctuations of the streamwise velocity component, u'_x, and of the cross-stream one, u'_y, normalized by the mean flow intensity U, for three selected probes. In these plots, time is normalized by the polymer relaxation time τ. Note that the data here reported correspond to a subset of the full time series, which extends to 800 τ. As one can clearly see, the temporal signals from different probes all
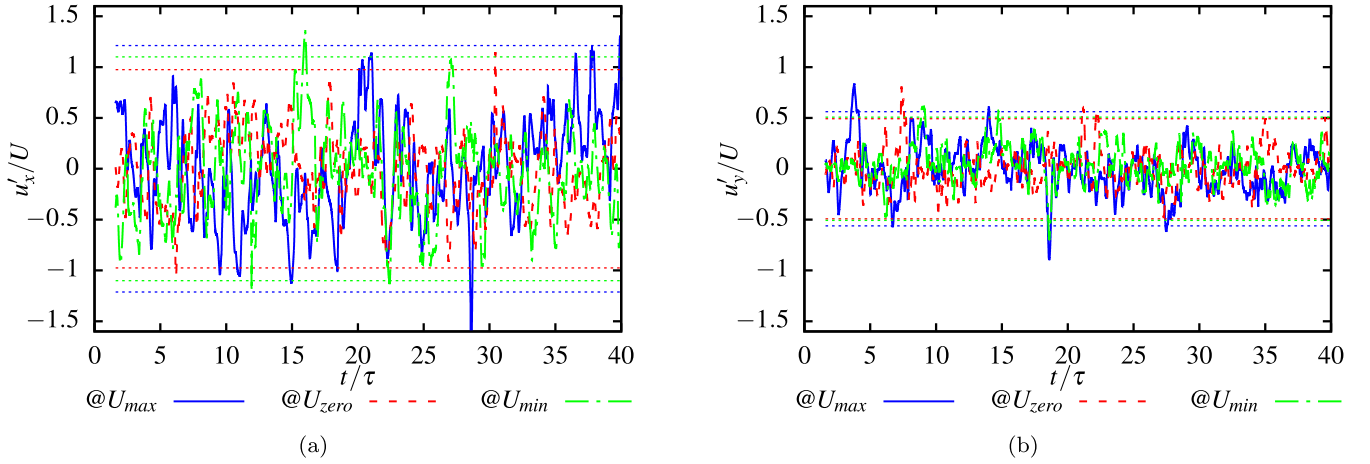
FIG. 3. Time series of u'_x (a) and u'_y (b), normalized by the mean flow amplitude U, at Wi = 24.9, as recorded by three different probes at the U_{max}, U_{zero}, and U_{min} locations. Horizontal dotted lines indicate $\overline{u'_{x,y}} \pm \sigma_{u'_{x,y}}$, where the overbar denotes a temporal average and $\sigma_{u'_{x,y}}$ the standard deviation with respect to it. To ease visualization, only a short subset of the full data set (which reaches $t/\tau = 800$) is shown.

share a common behavior, including that from the probe at zero-mean-flow location. It is also worth remarking the different intensity of fluctuations in the x and y directions, which we will address more in detail in subsequent sections.
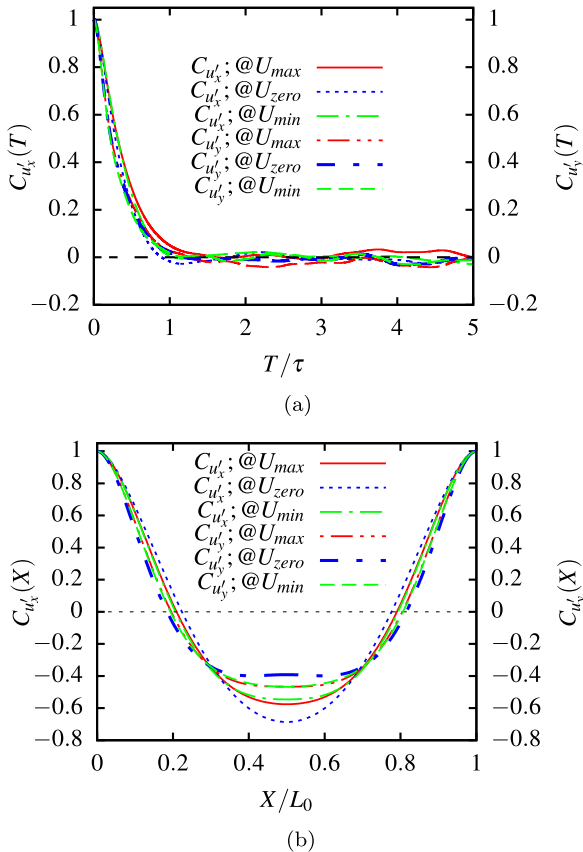

FIG. 4. Normalized temporal (a) and spatial (b) autocorrelation functions of u'_x (left axes) and u'_y (right axes). In both (a) and (b) data from probes where the mean flow is maximum, zero, and minimum are shown. The Weissenberg number is Wi = 24.9.

B. Temporal and spatial correlations of velocity fluctuations

Our measurements allow to quantitatively assess the correlations, in time and in space, of the fluctuating velocity field. Figure 4(a) shows the temporal correlation functions of the velocity fluctuation components,

$$C_{u'_i}(T) = \frac{\langle u'_i(t + T)u'_i(t)\rangle_t}{\langle [u'_i(t)]^2 \rangle_t}, \ i = x, y. \qquad (3)$$

The corresponding correlation times, computed as $t_{u'_i} = \int_0^{T_{max}} C_{u'_i}(T)dT$ are reported in Table I, where $T_{max} = \mathcal{O}(10^2)\tau$ is the duration of the largest time increment. Irrespective of the position of the probe, we find that the correlation times of the two velocity components are comparable, and their values are of the order of the polymer relaxation time τ. This is in agreement with the theory by Lebedev and collaborators [14] and experimental results [4].

The spatial correlation functions of each velocity component are defined as:

$$C_{u'_i}(X) = \frac{\langle u'_i(x + X)u'_i(x)\rangle_x}{\langle [u'_i(x)]^2 \rangle_x}, \ i = x, y, \qquad (4)$$

where the brackets indicate an average over the x direction and X is the distance between two points in the same direction. Here we only focus on such a streamwise direction, which seems to us more interesting, as in the cross-stream one (y), the typical length scale is clearly constrained by the periodic

TABLE I. Correlation times and correlation lengths (in the streamwise direction) of fluctuations of both velocity components. The correlation times are measured as $t_{u'_i} = \int_0^{T_{max}} C_{u'_i}(T)dT$, while the correlation lengths are deduced from the zero-crossing length of the corresponding autocorrelation functions $C_{u'_i}(X)$.

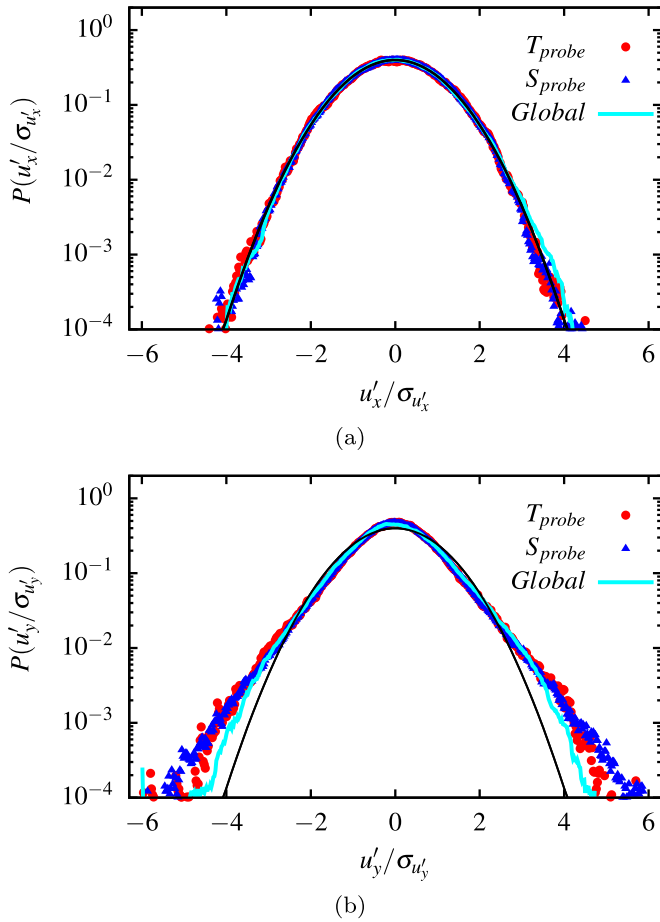|	$t_{u'_x}/\tau$	$t_{u'_y}/\tau$	$l_{u'_x}/L_0$	$l_{u'_y}/L_0$
@U_{max}	1.568	1.264	0.211	0.197
@U_{zero}	0.885	1.286	0.381	0.185
@U_{min}	1.040	1.558	0.207	0.197

FIG. 5. Probability distribution functions of (a) $u'_x/\sigma_{u'_x}$ and (b) $u'_y/\sigma_{u'_y}$ (with $\sigma_{u'_i}$ the rms values of u'_i and $i = x, y$) for Wi = 24.9. Red (circle) and blue (triangle) points respectively correspond to the PDFs for temporal and spatial probes, using data collected where the mean flow amplitude is maximum and minimum. Aqua color points (solid line) stand for the PDFs from global spatial data from 1000 instantaneous snapshots of velocity fields.

structure of the mean flow and is therefore roughly equal to $1/k = 1/4$ of the domain length.

We then determine the corresponding correlation lengths $l_{u'_i}$ as those for which the functions $C_{u'_i}(X)$ cross the zero line for the first time. The measured values are all quite close to $\approx 0.2L_0$ [see Fig. 4(b) and Table I], which is close to the wavelength of the forcing, but slightly larger for u'_x, particularly

where the mean flow vanishes, and the mean velocity gradient is largest.

C. Analysis of probability density functions

In this section, we focus on the PDF of velocity fluctuations, as well as of the corresponding accelerations $\partial_t u'_i$ and of the spatial gradients $\partial_x u'_i$. Based on these analyses, we will also address the validity of Taylor's hypothesis for the present flow.

1. PDF of velocity fluctuations

An advantage of our numerical approach, with respect to experiments, is the possibility to use also information sampled at different locations in the flow. Hence, in addition to the data from the temporal probes (T_{probes}) introduced earlier, in the following we will also consider data extracted along lines in the streamwise direction (for fixed y values corresponding to maximum, zero and minimum mean flow), as done for the correlation functions discussed in Sec. III B. Aiming to compare the statistics from these data with those from single fixed-point measurements, we will refer to such data extractions as spatial probes (S_{probes}) (see Fig. 1). The results already presented indicate a weak dependence of the statistical features of the flow from the position where the data are collected. For this reason, in order to enlarge the size of our samples, we will analyze together the data from probes in locations of maximum and minimum mean flow, and we will also consider global statistics, meaning obtained from all points in space (though for less instants of time).

In Fig. 5 we present the PDFs of both longitudinal and transversal velocity fluctuations for the data from temporal probes and spatial ones (both locally and globally). Note that here the fluctuations are scaled by their root-mean-square (rms) value. In the present regime of fully developed elastic turbulence all the considered distributions of longitudinal velocity fluctuations are found to be well described by a Gaussian function with very little skewness [Fig. 5(a)]. In the transversal direction, the differently sampled PDFs are still close to each other, but we detect a slight deviation from Gaussianity, particularly for large fluctuations [Fig. 5(b)]. These curves are symmetric within our numerical accuracy. The values of different order moments (mean, $\langle \ldots \rangle$, standard deviation, σ, skewness, A, and kurtosis, K) of both u'_x and u'_y, measured from temporal statistics, are reported in Table II.

The probability distribution of Eulerian acceleration fluctuations $\partial_t u'_i = \frac{u'_i(t+\delta t) - u'_i(t)}{\delta t}$ (with $i = x, y$) computed by finite

TABLE II. Moments of velocity fluctuations (u'_x and u'_y): mean, $\langle \ldots \rangle$; standard deviation, σ; skewness, A; and kurtosis, K. In the last two columns we also report the turbulence intensities for both velocity components, $I_{u'_x}$ and $I_{u'_y}$. All the values in this table are obtained from temporal probes at locations of maximum, zero and minimum mean flow. The last line corresponds to the global statistics. Note that the turbulence intensities are not defined in the absence of mean flow.

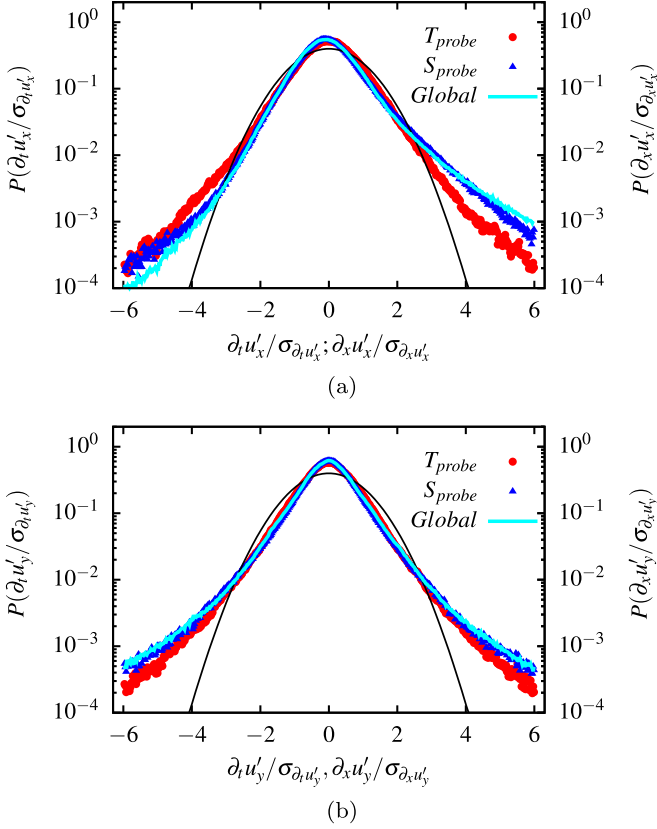| T_{probes}	$\langle u'_x \rangle$	$\sigma_{u'_x}$	$A_{u'_x}$	$K_{u'_x}$	$\langle u'_y \rangle$	$\sigma_{u'_y}$	$A_{u'_y}$	$K_{u'_y}$	$I_{u'_x}$	$I_{u'_y}$
@U_{max}	2.469	1.186	−0.059	2.831	−0.002	0.500	0.042	4.235	0.480	0.202
@U_{zero}	−0.003	0.955	0.050	3.219	−0.001	0.570	0.020	4.295		
@U_{min}	−2.460	1.170	0.068	2.794	−0.010	0.495	−0.046	3.995	0.476	0.201
Global	−8.132×10⁻⁰⁸	1.034	0.020	2.789	4.142×10⁻¹⁰	0.508	0.063	3.780		

(a)

(b)

FIG. 6. Probability distribution functions of acceleration fluctuations $\partial_t u'_i / \sigma_{\partial_t u'_i}$ [red points (circle), from temporal probes], and of velocity-gradient fluctuations $\partial_x u'_i / \sigma_{\partial_x u'_i}$, measured from both spatial probes [blue points (triangle)] and from global spatial data [aqua color points (solid line)], for Wi = 24.9. All variables are scaled by their rms value σ. Panels (a) and (b) refer to the x and y components of velocity, respectively. The temporal and spatial probes are located where the mean flow is maximum and minimum, the global statistics make use of data from 1000 instantaneous velocity fields.

differences with a temporal increment δt, scaled by the rms value, is shown in Fig. 6 [red points (circle), from temporal probes]. For both x and y components, the PDFs deviate from the Gaussian distribution, especially for large fluctuations, providing evidence of intermittent behavior at small scales. The situation of nearly Gaussian statistics of velocities and essentially non-Gaussian, high-tail distributions of velocity derivatives, is similar to what occurs in high-Re inertial turbulence [29]. This result is also consistent with the measurements performed in different ET geometrical setups [4,17], but note that the PDFs of velocity derivatives (Fig. 6) display slight deviations from the exponentially tailed shape

found in experiments. For completeness, as for the velocity statistics, the values of different order moments of acceleration statistics, measured from temporal probes, are reported in Table III.

2. The Taylor's frozen-field hypothesis and the PDF of velocity gradients

We now address the validity of Taylor's hypothesis in the present 2D elastic turbulence model system. Taylor's hypothesis states that for any quantity, ϕ, transported in a turbulent flow and measured at different times (t and $t + T$) at a fixed location in space (x), the relation between temporal and spatial increments is the following:

$$\phi(t+T) - \phi(t) = \phi(x - UT) - \phi(x), \quad (5)$$

where U is the mean velocity at the measurement location, x is the spatial coordinate in the direction of the mean flow. This is equivalent to say that the conversion between temporal (T) and spatial (X) increments is $X = U\,T$ and it justifies dubbing it Taylor's frozen-field hypothesis (TH). In the limit of vanishing increments T Eq. (5) leads to

$$\partial_t \phi = -U\,\partial_x \phi. \quad (6)$$

Note that the TH works also when the transported quantity is the turbulent velocity fluctuation itself, u'_i or a function of it, such as the turbulent kinetic energy.

Equations (5) and (6) are commonly used, in experimental studies, to evaluate the streamwise spatial increments or derivative of ϕ, given its finite increments or time derivative. This is done by necessity since fully resolved flow-field measurements, in space, are notably difficult and require sophisticated experimental techniques. Besides the statistical steadiness of the flow the main requirement for the validity of TH is the existence of a large local mean velocity, as compared to velocity fluctuations [30]:

$$\frac{u'}{U} \ll 1. \quad (7)$$

The extent to which TH is expected to hold, in general flow conditions, has been discussed theoretically [31–33]. However, this point needs, in principle, to be checked on a case-by-case basis in experiments and numerical simulations.

A large body of experimental works addressed the subject, mainly in relation to 2D and 3D inertial turbulent flows [34–37]. In particular, detailed discussions have been devoted to the applicability of TH for flows with strong shear and high turbulence intensities [33,34,37–41]. Using accurate time-dependent measurements of the flow field, the degree of validity of TH was assessed in experiments of elastic turbu-

TABLE III. Moments of acceleration fluctuations ($\partial_t u'_x$ and $\partial_t u'_y$): mean, $\langle \ldots \rangle$; standard deviation, σ; skewness, A; and kurtosis, K. All the values in this table are obtained from temporal probes at locations of maximum, zero, and minimum mean flow.

T_{probes}	$\langle \partial_t u'_x \rangle$	$\sigma_{\partial_t u'_x}$	$A_{\partial_t u'_x}$	$K_{\partial_t u'_x}$	$\langle \partial_t u'_y \rangle$	$\sigma_{\partial_t u'_y}$	$A_{\partial_t u'_y}$	$K_{\partial_t u'_y}$
@U_{max}	0.022	4.922	0.637	15.925	0.000	2.869	−0.032	12.633
@U_{zero}	−0.000	4.097	−0.060	8.423	−0.000	3.200	−0.042	10.753
@U_{min}	0.021	4.933	0.704	16.684	−0.001	2.910	0.049	12.736

TABLE IV. Moments of the longitudinal gradients of velocity fluctuations ($\partial_x u'_x$ and $\partial_x u'_y$): mean, $\langle \ldots \rangle$; standard deviation, σ; skewness, A; and kurtosis, K. All the values in this table are obtained from local spatial probes at locations of maximum, zero and minimum mean flow, global statistics, and averaging over time.

S_{probe}	$\langle \partial_x u'_x \rangle$	$\sigma_{\partial_x u'_x}$	$A_{\partial_x u'_x}$	$K_{\partial_x u'_x}$	$\langle \partial_x u'_y \rangle$	$\sigma_{\partial_x u'_y}$	$A_{\partial_x u'_y}$	$K_{\partial_x u'_y}$
@U_{max}	2.982×10^{-10}	1.292	0.909	8.032	-6.535×10^{-11}	1.004	0.048	6.001
@U_{zero}	-1.220×10^{-10}	1.220	0.976	7.127	6.138×10^{-12}	0.902	0.015	5.120
@U_{min}	-1.074×10^{-10}	1.234	0.923	7.234	-7.582×10^{-11}	0.894	-0.059	5.262
Global	-4.692×10^{-12}	1.240	0.763	6.292	-2.958×10^{-12}	0.965	-0.036	6.086

lence, by examining the velocity coherence of pairs of points separated by both spatial and temporal intervals [18].

To test the validity of the frozen-field hypothesis, one can either measure the velocity correlation functions or, in light of Eq. (6), compare the accelerations $\partial_t u'_i$ with the velocity gradients $\partial_x u'_i$. These two approaches are complementary: The correlation-based method is conditioned by the spatial resolution of the velocity fields, whereas the second one requires a high temporal resolution. Here we consider the second approach, choosing to compare the probability distribution functions of the temporal and spatial derivatives of velocity fluctuations.

To check whether the velocity fluctuations are transported without evolving dynamically, the essential meaning of TH, we compute the spatial gradients of each component of the velocity fluctuations along the streamwise direction of the flow, and compare them to the Eulerian accelerations previously calculated [see Fig. 6, where blue points (triangle) correspond to spatial probes and aqua color (solid line) ones to global statistics]. Table IV provides a summary of the values measured for different order moments for both components of (longitudinal) spatial gradients. The magnitude of the typical gradients at the present Weissenberg number, estimated from their standard deviations, is roughly of order $1/\tau$, in reasonable agreement with theoretical predictions [14] and independent measurements based on the Lagrangian Lyapunov exponent of the flow [8].

Inspection of Fig. 6 reveals different statistical behaviors of temporal and spatial derivatives of the velocity fluctuations, at least for the flow component in the streamwise direction [Fig. 6(a)]. Indeed, while the distributions from both temporal and spatial probes exhibit high tails indicative of intermittency, the PDF of $\partial_x u'_x$ is found to be more positively skewed. Such a discrepancy is not in agreement with Eq. (6) and, therefore, provides a first evidence of a partial breakdown of TH.

Further support to the differences observed above comes from an analysis of third-order statistics. The behavior of $|z|^3 P(z)$, with z the variable of interest and $P(z)$ the corresponding PDF [and $\int z^3 P(z) dz$ the third-order moment of $P(z)$], is shown in Fig. 7 for velocity fluctuations, and in Fig. 8 for the temporal/spatial derivatives of the latter. The velocity statistics from spatial and temporal data are essentially indistinguishable (Fig. 7). Figure 8, instead, shows major differences between the statistics of the local accelerations $\partial_t u'_i$ and those of the corresponding spatial gradients, especially for the streamwise component $\partial_x u'_x$. A similar study on fourth, and higher, order statistics could not be carried out because of still limited convergence of the spatial data. In spite of these

limitations, the above results provide, in our opinion, a clear indication of the fact that, in our flow, spatial and temporal probes sample different statistics, implying that TH cannot be considered to be satisfied.

To conclude this discussion, we note *a posteriori*, that such findings are consistent with the estimates of the turbulent intensities $I_{u_i} = \sigma_{u'_i}/U$, whose values, for both the x and y flow components, are reported in Table II. We find, indeed, that the typical fluctuations' intensities are not negligible with
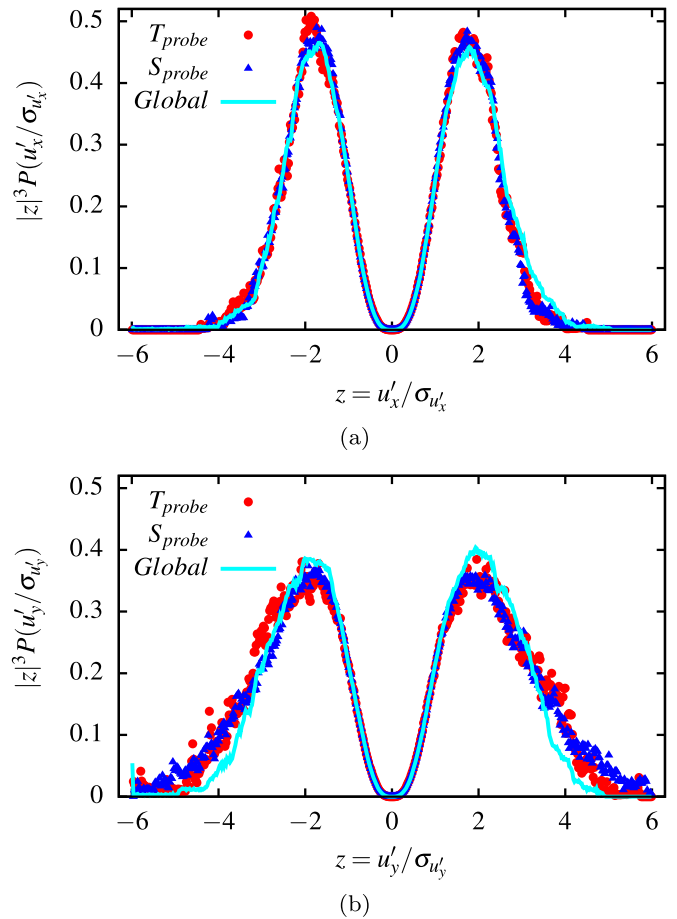

(a)

(b)

FIG. 7. Third-order statistics $|z|^3 P(z)$ for $z = u'_x/\sigma_{u'_x}$ (a) and $z = u'_y/\sigma_{u'_y}$ (b), for Wi = 24.9. Red (circle) and blue (triangle) points respectively correspond to data from temporal and spatial probes, located where the mean flow is maximum and minimum; aqua color points (solid line) correspond to global spatial data. All spatial statistics are further averaged over time using 1000 instantaneous velocity fields.
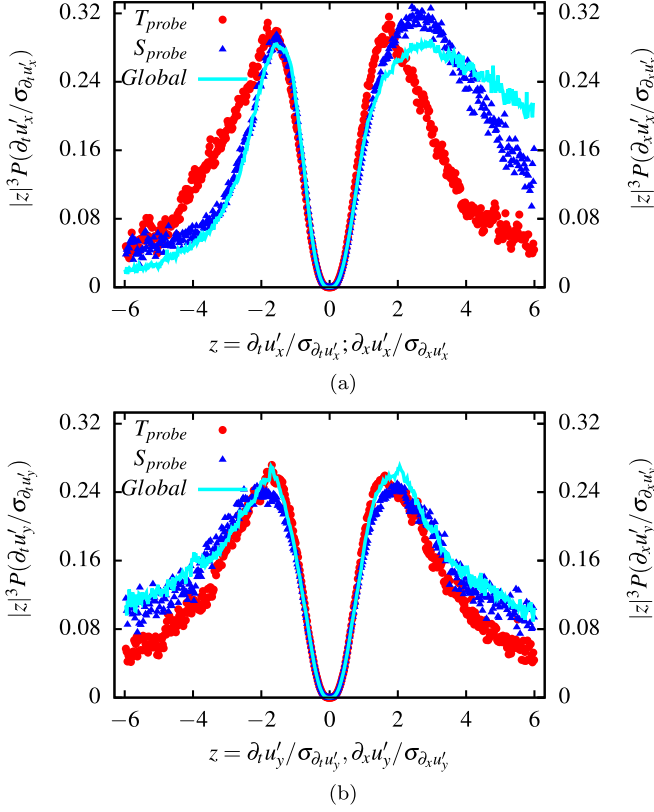
FIG. 8. Third-order statistics $|z|^3 P(z)$ for $z = \partial_t u_i'$ (local accelerations) and $z = \partial_x u_i'$ (longitudinal gradients) for Wi = 24.9. Panel (a) refers to the streamwise velocity component ($i = x$), panel (b) to the cross-stream one ($i = y$). Red (circle) and blue (triangle) points respectively correspond to data from temporal and spatial probes, located where the mean flow is maximum and minimum; aqua color points (solid line) correspond to global spatial data. All spatial statistics are further averaged over time using 1000 instantaneous velocity fields.

respect to the mean flow. They are close to $0.2\,U$ in the cross-stream direction and reach $\approx 0.5\,U$ in the streamwise one, showing that the condition in Eq. (7) is not fulfilled. Important velocity fluctuations, in comparison to the mean flow, have been reported also in simulations of elastic turbulence in different geometry [27]. It is worth noting, however, that the present observation shares some similarity also with the behavior occurring in the 3D Newtonian Kolmogorov flow at high Reynolds number [42]. This likely indicates that the specific values of the turbulence intensities found here may be due to the present, unbounded, geometrical configuration.

D. Two-point finite-increment statistics

We now present the results of our analysis based on spectra and structure functions. By means of the latter, we will also address the isotropy properties of the flow at different length scales.

1. Spectra of velocity fluctuations

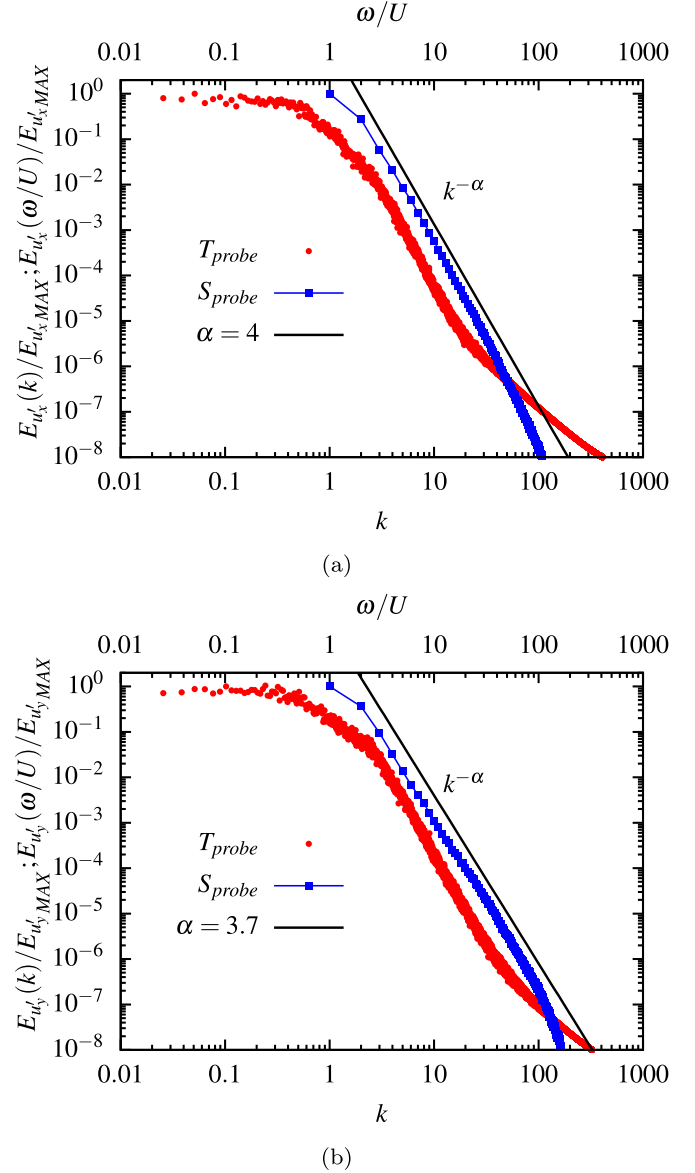Using fixed-point temporal measurements, we compute power spectra of velocity fluctuations, in the frequency (f)

FIG. 9. Spectra of velocity fluctuations u_x' (a) and u_y' (b) from temporal and spatial data from probes located where the mean flow is maximum and minimum for Wi = 24.9. The bottom horizontal axis refers to the spatial spectra, the top one refers to temporal spectra, after conversion, where $\omega = 2\pi f$, f is the frequency and U the mean flow intensity. All spectra in (a) and (b) are normalized by their maximum values.

domain, at different probe locations. Aiming to compare them with unidimensional spectra, in the wave-number (k) domain, computed from the corresponding spatial probes, we convert them to spatial spectra, ignoring the limited validity of TH for our flow. The resulting spectra ($E_{u_i'}$), of both type (from temporal and spatial probes), are reported in Fig. 9, with Figs. 9(a) and 9(b) showing the spectra of u_x' and u_y', respectively. In both cases, and independently of the considered flow component, we find power-law decaying spectra $E_{u_i'}(f) \sim f^{-\alpha}$ and $E_{u_i'}(k) \sim k^{-\alpha}$, with a common exponent $\alpha \approx 4$. The scaling range extends over almost two decades for the spatial spectra, and slightly less for the temporal ones.

The nonoverlapping of temporal and spatial spectra, after appropriate conversion, reflects the limited validity of TH. The similar behavior of $E_{u'_i}(f)$ and $E_{u'_i}(k)$, however, suggests that the latter may be still used as a working hypothesis, depending on what statistical features one focuses on. Finally, we note that similarly steep spectra have been found in experiments [1,17], in the frequency domain, and theoretically predicted assuming homogeneity and isotropy [14], in the wave-number domain. Such a similarity is intriguing, considering that both the theory and experiments deal with 3D flows, and calls for further studies on the role of the space dimensionality in ET.

2. Second-order structure functions and isotropy

We are interested in assessing the isotropy properties of the flow at different length scales. At large scales, the flow is anisotropic, as evidenced by the different rms values of velocity fluctuations in the two directions (Table II). A natural question then is if isotropy is recovered at smaller scales. To explore this point, we consider the second-order spatial velocity structure functions:

$$S^{(2)}_{u'_i}(X) = \langle |u'_i(x + X, y, t) - u'_i(x, y, t)|^2 \rangle_{x,y,t}, \qquad (8)$$

with $i = x, y$, where X is an increment in the streamwise direction and $\langle \ldots \rangle_{x,y,t}$ indicates averaging over the spatial positions (x, y) and the time t. The positions (x, y) are taken either over all the volume in the case of *global* structure functions or over lines at fixed y coordinate corresponding to the positions of mean flow maxima and minima, in the so-called spatial probe, S_{probe}, case (see Fig. 1). Similarly, for temporal probes, T_{probe}, we use a definition analogous to (8) but for time increments at fixed (x) locations:

$$S^{(2)}_{u'_i}(T) = \langle |u'_i(x, y, t + T) - u'_i(x, y, t)|^2 \rangle_{y,t}, \qquad (9)$$

where the average is now over the set of T_{probes} positioned at the flow maxima and minima U_{max}, U_{min}. The temporal increments can be converted to length increments by invoking TH, via the mean flow intensity $X = UT$.

Let us first comment on the general behavior found for such structure functions. The results of our measurements are reported in Fig. 10(a) for $S^{(2)}_{u'_x}$ and Fig. 10(b) for $S^{(2)}_{u'_y}$. From these plots, we can see that $S^{(2)}_{u'_i} \sim X^2$, meaning that the flow is smooth, which is consistent with spatial spectra being steeper than k^{-3}. Moreover, as for spectra, the curves from temporal and spatial probes do not overlap, even after rescaling. Indeed, to let them superpose one would need a reduced value $\hat{U} < U = 2.5$, specifically $\hat{U} \simeq 1.9$ for u'_x and $\hat{U} \simeq 1.6$ for u'_y. This further confirms that TH does not hold in the present setup. The tiny mismatch between the *Global* and S_{probe} functions is originated by the weak statistical nonhomogeneity present in the system. This nonhomogeneity, however, does not affect the scaling properties.

By taking into account the statistical stationarity of the flow, the incompressibility condition and the flow isotropy, one can derive the relation between parallel $S^{(2)}_{//}(r) = \langle [u(x + r, t) - u(x, t)] \cdot \hat{r})^2 \rangle_{x,t}$ and perpendicular $S^{(2)}_{\perp}(r) = \langle [u(x + r, t) - u(x, t)] \cdot \hat{n})^2 \rangle_{x,t}$ second-order spatial structure functions for a given increment $r = r\hat{r}$ and with $\hat{n}$ the unit vector normal to $\hat{r}$, i.e., $\hat{n} \cdot \hat{r} = 0$. In a 2D flow this reads:
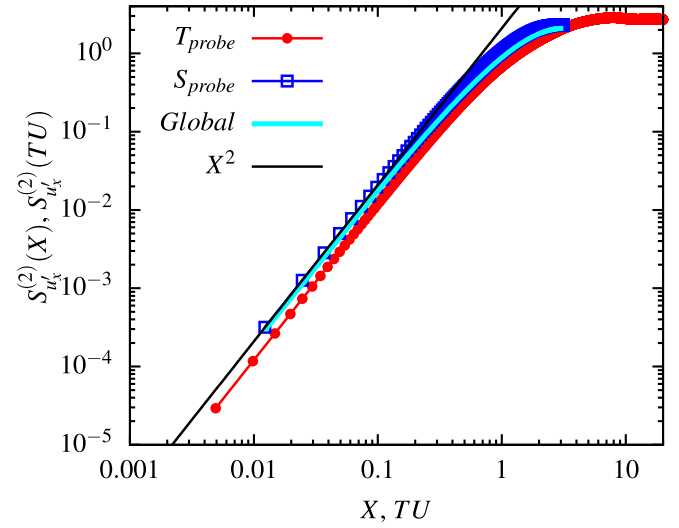
(a)
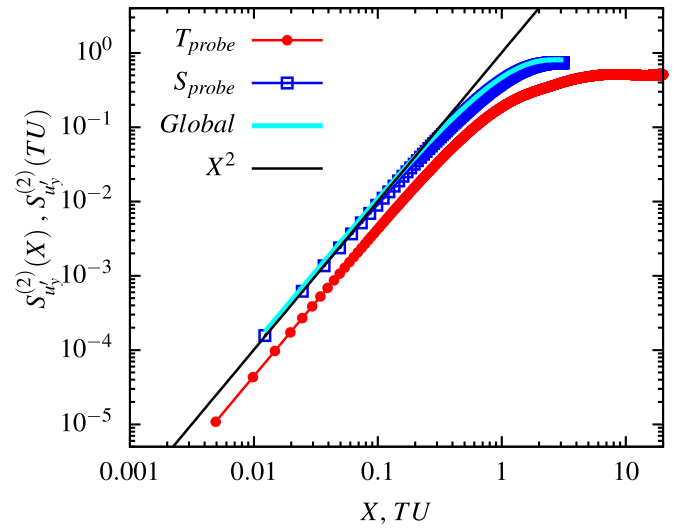
(b)

FIG. 10. Second-order velocity structure functions, for Wi = 24.9, versus the spatial increment (either measured directly, X, or via the mean flow intensity, TU). Panel (a) refers to u'_x, panel (b) refers to u'_y. Red (circle) and blue (square) points respectively correspond to data from temporal and spatial probes, located where the mean flow is maximum and minimum; aqua color points (solid line) are for global statistics. Spatial statistics are further averaged over time using 1000 instantaneous velocity fields.

$r \frac{d}{dr} S^{(2)}_{//}(r) + S^{(2)}_{//}(r) = S^{(2)}_{\perp}(r)$ (see the complete derivation in the Appendix), which implies:

$$X \frac{d}{dX} S^{(2)}_{u'_x} + S^{(2)}_{u'_x} = S^{(2)}_{u'_y}, \qquad (10)$$

or

$$\frac{d}{dX} \left[X S^{(2)}_{u'_x} \right] = S^{(2)}_{u'_y}. \qquad (11)$$

We can now observe that in the case of a smooth flow Eq. (11), at sufficiently small X, leads to $3S^{(2)}_{u'_x} \simeq S^{(2)}_{u'_y}$. This
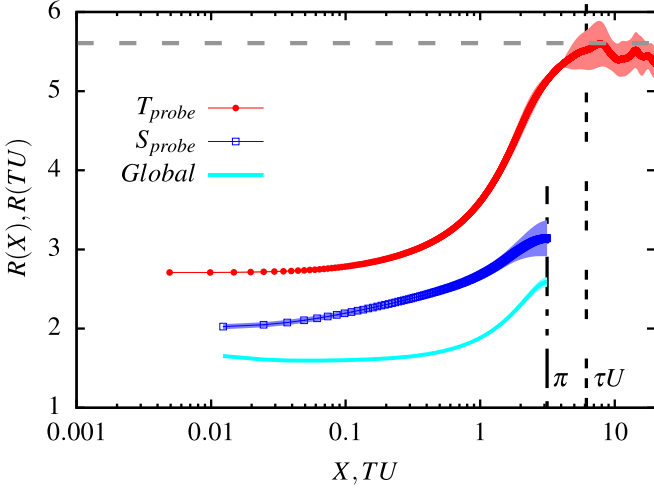
FIG. 11. Isotropy ratio, $R = S_{u'_x}^{(2)}/S_{u'_y}^{(2)}$, versus the spatial increment (either measured directly, X, or via the mean flow intensity, TU), for Wi = 24.9. Red (circle) and blue (square) points respectively correspond to data from temporal and spatial probes, located where the mean flow is maximum and minimum; aqua color points (solid line) are for global statistics. All spatial statistics are further averaged over time using 1000 instantaneous velocity fields. The horizontal dashed gray line corresponds to the value of $\sigma_{u'_x}^2/\sigma_{u'_y}^2$ obtained from temporal probes (Table II). The vertical long-short dashed black line represents the largest possible increment, $L_0/2 = \pi$. The vertical dashed black line represents the length scale corresponding to a time $t = \tau$. Error bars are estimated by dividing the data sets into two equal parts.

can be also understood as the limit where $S_{u'_i}^{(2)} = \sigma_{\partial_x u'_i}^2 X^2$ and, hence, $S_{u'_x}^{(2)}/S_{u'_y}^{(2)} \approx \sigma_{\partial_x u'_x}^2/\sigma_{\partial_x u'_y}^2$. Such a ratio of the velocity gradients' variances is then expected to attain the value $1/3$ in isotropic conditions in 2D flows, as also shown in Ref. [43] (while it is $1/2$ in 3D flows, see also the Appendix). In the, opposite, large-scale limit ($X \to L_0/2$ or $T \to +\infty$) the structure functions should reach a constant value. This can originate either as an artifact of the periodicity of the system (at increments $X = L_0/2$ the structure functions' slopes are 0 by construction) or by a genuine decorrelation of velocity fluctuations beyond a given scale. In the latter case the velocity fluctuations will not be correlated anymore over such large increments and, consequently, from Eq. (8) one has $S_{u'_i}^{(2)}(X) \sim 2\langle u'^2_i \rangle = 2\sigma_{u'_i}^2$.

To test the degree of isotropy of the flow and its scale dependence, we examine the ratio

$$R(X) = S_{u'_x}^{(2)}(X)/S_{u'_y}^{(2)}(X), \qquad (12)$$

which is reported in Fig. 11 as a function of the increment X and again, we consider data from both spatial probes and temporal ones, computed as described above. Our results indicate that isotropy is not recovered at small scales, as for all data sets $R(X)$ is much larger than the theoretical expectation of $1/3$. At large scales, as expected, we find anisotropic fluctuations, as the data do not approach the expected limit $\sigma_{u'_x}^2/\sigma_{u'_y}^2 \approx 1$. The isotropy ratio from temporal probes' signals reaches the limit $\sigma_{u'_x}^2/\sigma_{u'_y}^2 \approx 5.6$ (dashed gray curve in Fig. 11, obtained

from the values in Table II). The limit is attained for times larger than the polymer relaxation time τ, beyond which velocity fluctuations then result to be uncorrelated, in agreement with our previous observation (see Sec. III B). Interestingly, however, the figure also reveals that velocity increments from spatial statistics, both *Global* and S_{probe} ones, appear to be still correlated at the largest possible value of the increment ($X = L_0/2 = \pi$), as in this case $R(X)$ does not reach the ratio of velocity variances, which should be again ≈ 5.6 for S_{probe} data and ≈ 4 for *Global* ones (Table II).

We conclude this section by noting, once more, the lack of correspondence between spatial and temporal statistics for the flow studied here.

3. Skewness of velocity increments

In this last section we want to reconsider the asymmetry observed in the PDFs of Fig. 6. In particular we aim at quantifying the normalized third-order moment of velocity increments at different scales. For this purpose we compute the scale-dependent quantity

$$A_i(X) = S_{u'_i}^{(3)}(X)/\left[S_{u'_i}^{(2)}(X)\right]^{3/2}, \quad i = x, y, \qquad (13)$$

where $S_{u'_i}^{(2)}$ is the second-order structure function defined in Eq. (8) and $S_{u'_i}^{(3)}$ is the third-order structure function, defined analogously. The function $A_i(X)$ in Eq. (13) can be seen as a scale-by-scale skewness of velocity increments and its limit for $X \to 0$ gives the skewness of the velocity gradient $A_{\partial_x u'_i}$. Again, we make use of data from both spatial probes (locally and globally) and temporal ones, with time converted to space using the mean flow intensity U (as in the previous section).

The results are presented in Fig. 12, where Fig. 12(a) and 12(b) respectively refer to u'_x and u'_y. While the skewness of the cross-stream-velocity increments is essentially zero at all scales [Fig. 12(b)], and independently of how the data are sampled, this is not always the case for the streamwise velocity. In that case in fact, only the measurement from temporal probes gives zero, scale-independent, skewness. As it can be seen from Fig. 12(a), for decreasing X, $A_x(X)$ (from spatial data) grows to attain a positive constant value, at the smallest increments, compatible with the PDFs in Fig. 6(a) (and the value of $A_{\partial_x u'_x}$ from Table IV). We shall stress here that no skewness is expected for the distribution of $\partial_x u'_x$ in inertial high-Reynolds isotropic 2D flows, as a consequence of Karman-Howarth equation [44]. We do not have, at present, a clear explanation for the origin of the skewness in our data. Nevertheless, we point out that these findings are in overall agreement with the analyses previously presented and indicate, through the different behaviors detected when using spatial or temporal data, that TH cannot be considered to be valid, over a whole range of scales. This, in turn, implies that temporal statistics are not apt to capture the fine statistical features of the flow, as those quantified by the third-order moment (and most likely by higher-order ones).

IV. CONCLUSIONS

We have presented a systematic numerical investigation of the statistical properties of a smooth random flow of a
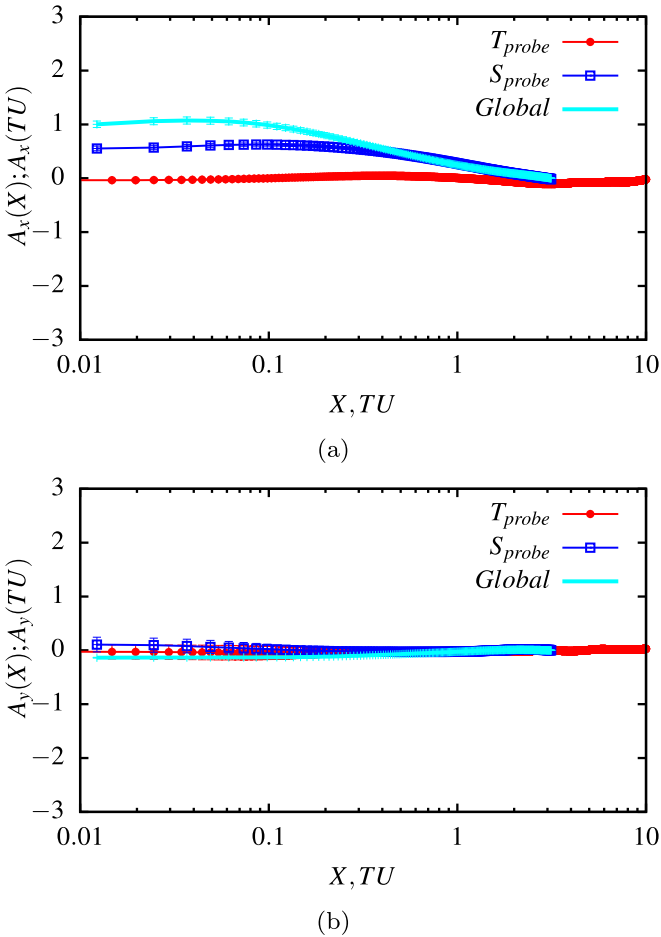
FIG. 12. Scale-dependent skewness $A_i = S^{(3)}_{u'_i}(X)/[S^{(2)}_{u'_i}(X)]^{3/2}$ versus the spatial increment (either measured directly, X, or via the mean flow intensity, TU). Panel (a) refers to u'_x and panel (b) refers to u'_y. Red (circle) and blue (square) points respectively correspond to data from temporal and spatial probes, located where the mean flow is maximum and minimum; aqua color points (solid line) are for global statistics. All spatial statistics are further averaged over time using 1000 instantaneous velocity fields. For all the data shown the error bar, estimated by dividing the data sets into two equal parts, is of the order of the point size.

dilute polymer solution resulting from the dynamics of the 2D viscoelastic Kolmogorov flow in the regime of elastic turbulence [8].

By means of accurate temporal and spatial measurements, we find nearly Gaussian statistics of velocity fluctuations, and essentially non-Gaussian distributions, indicative of intermittency, of velocity gradients. These results are in overall qualitative agreement with experimental ones [4,17], and return a picture resembling the phenomenology occurring in inertial turbulence at high Reynolds numbers [29].

The sampled statistics are, to good extent, homogeneous and only weakly depend on the location of the measurement. We provide evidence, however, that in our system the streamwise and cross-stream components of the velocity fluctuations do not behave equally. Indeed, our results indicate that the flow is anistropic from the largest scales, where the external

forcing acts, down to the smallest ones, and for very small time lags.

The central conclusion of our study is that, in spite of the presence of a well-defined mean flow, in this system Taylor's frozen-field hypothesis does not fully apply. On one side, we find important velocity fluctuations, as compared to the mean-flow intensity, a feature in common with the 3D Newtonian turbulent Kolmogorov flow [42]. On the other side, we systematically find differences in the statistical properties computed by sampling the data in time or in space.

This fact does not reveal dramatic, as long as the focus is on the scaling properties of the spectra of velocity fluctuations, which are essentially identical in the frequency and wave-number domains. However, as shown by our detailed investigation, statistics sampled in time do not seem to allow capturing finer features here, as those quantified by higher-order moments like the skewness of velocity increments. The present results then suggest that caution should be used when examining intermittency properties based on information from temporal sampling only.

We hope that the analysis reported in this work may help to establish sound methodologies to compare in detail numerical simulations of elastic turbulence with the available experimental results [1,4,6,9]. This type of fine-scale comparisons appear to us crucial to improve the theoretical understanding on the subject and to validate the related numerical developments.

APPENDIX: STATISTICAL ISOTROPY IN TWO DIMENSIONS AND SECOND-ORDER STRUCTURE FUNCTIONS

The correlation tensor of velocity fluctuations, $\boldsymbol{u}'$ in its not-normalized form is defined as:

$$R_{ij}(\boldsymbol{r}) = \langle u'_i(\boldsymbol{x}+\boldsymbol{r},t)u'_j(\boldsymbol{x},t)\rangle, \quad (A1)$$

where $\boldsymbol{r}$ is a generic increment of magnitude $r = ||\boldsymbol{r}||$ and orientation $\hat{\boldsymbol{r}} = \boldsymbol{r}/r$, and the average is taken over space and time in statistically stationary conditions (and thus the time dependence in R_{ij} is dropped).

The assumption of statistical isotropy for this second-order tensorial function can be written as:

$$R_{ij}(r) = \mathcal{A}(r)\hat{r}_i\hat{r}_j + \mathcal{B}(r)\delta_{ij}. \quad (A2)$$

Following Batchelor [45] we define the longitudinal (or parallel) and the transversal (or perpendicular) correlation functions

$$R_{//}(r) = \langle[\boldsymbol{u}'(\boldsymbol{x}+\boldsymbol{r},t)\cdot\hat{\boldsymbol{r}}][\boldsymbol{u}'(\boldsymbol{x},t)\cdot\hat{\boldsymbol{r}}]\rangle, \quad (A3)$$

$$= R_{ij}\hat{r}_i\hat{r}_j = \mathcal{A}(r) + \mathcal{B}(r) = f(r), \quad (A4)$$

and

$$R_{\perp}(r) = \langle[\boldsymbol{u}'(\boldsymbol{x}+\boldsymbol{r},t)\cdot\hat{\boldsymbol{n}}][\boldsymbol{u}'(\boldsymbol{x},t)\cdot\hat{\boldsymbol{n}}]\rangle, \quad (A5)$$

$$= \mathcal{B}(r) = g(r), \quad (A6)$$

where $\hat{\boldsymbol{n}}$ is a unit vector perpendicular to $\hat{\boldsymbol{r}}$. Using (A4) and (A6), Eq. (A2) can be rewritten as

$$R_{ij}(r) = (f-g)\hat{r}_i\hat{r}_j + g(r)\delta_{ij}. \quad (A7)$$

Further, we note that the continuity condition $\partial_i u_i' = 0$ implies that $\frac{\partial}{\partial r_i} R_{ij}(r) = 0$ [45]. By using the chain rule of derivation, from (A7) we reach:

$$\frac{\partial}{\partial r_i} R_{ij}(r) = 0 = \hat{r}_j \left[\frac{d}{dr} f + \frac{(f-g)}{r} \right]. \quad (A8)$$

Since the above relation has to be true for any $\hat{r}_j$, this implies that the term between parentheses should be always zero, and so:

$$r \frac{df}{dr} + f = g, \quad (A9)$$

which is consistent with Davidson's developments (see Ref. [44], p. 597).

Finally, considering the relation between the correlation functions and the structure functions:

$$S_{//}^{(2)}(r) = 2[\sigma_{u_{//}'}^2 - f(r)], \ S_{\perp}^{(2)}(r) = 2[\sigma_{u_{\perp}'}^2 - g(r)], \quad (A10)$$

where $\sigma_{u_{//}'}^2 = \sigma_{u_{\perp}'}^2$ are the variances of the longitudinal and transversal velocity fluctuations (equal under isotropy), we obtain the notable result:

$$r \frac{d}{dr} S_{//}^{(2)}(r) + S_{//}^{(2)}(r) = S_{\perp}^{(2)}(r). \quad (A11)$$

We shall observe that the derivation of Eq. (A8) assumes a 2D space, where $\delta_{ii} = 2$. As a consequence, this result is different from the corresponding 3D expression, which takes the more familiar form [45]:

$$\frac{\partial}{\partial r_i} R_{ij}(r) = 0 = \hat{r}_j \left[\frac{d}{dr} f + 2 \frac{(f-g)}{r} \right],$$

implying

$$\frac{r}{2} \frac{d}{dr} S_{//}^{(2)}(r) + S_{//}^{(2)}(r) = S_{\perp}^{(2)}(r).$$

[1] A. Groisman and V. Steinberg, Elastic turbulence in a polymer solution flow, Nature (Lond.) **405**, 53 (2000).

[2] A. Groisman and V. Steinberg, Efficient mixing at low Reynolds numbers using polymer additives, Nature (Lond.) **410**, 905 (2001).

[3] L. Pan, A. Morozov, C. Wagner, and P. E. Arratia, Nonlinear Elastic Instability in Channel Flows at Low Reynolds Numbers, Phys. Rev. Lett. **110**, 174502 (2013).

[4] A. Souliès, J. Aubril, C. Castelain, and T. Burghelea, Characterisation of elastic turbulence in a serpentine micro-channel, Phys. Fluids **29**, 083102 (2017).

[5] P. C. Sousa, F. T. Pinho, and M. A. Alves, Purely-elastic flow instabilities and elastic turbulence in microfluidic cross-slot devices, Soft Matter **14**, 1344 (2018).

[6] V. Steinberg, Elastic turbulence: An experimental view on inertialess random flow, Annu. Rev. Fluid Mech. **53**, 27 (2021).

[7] T. Burghelea, E. Segre, I. Bar-Joseph, A. Groisman, and V. Steinberg, Chaotic flow and efficient mixing in a microchannel with a polymer solution, Phys. Rev. E **69**, 066305 (2004).

[8] S. Berti, A. Bistagnino, G. Boffetta, A. Celani, and S. Musacchio, Two-dimensional elastic turbulence, Phys. Rev. E **77**, 055306(R) (2008).

[9] T. Burghelea, E. Segre, and V. Steinberg, Elastic turbulence in von Karman swirling flow between two disks, Phys. Fluids **19**, 053104 (2007).

[10] B. Traore, C. Castelain, and T. Burghelea, Efficient heat transfer in a regime of elastic turbulence, J. Non-Newton. Fluid Mech. **223**, 62 (2015).

[11] W. M. Abed, R. D. Whalley, D. J. C. Dennis, and R. J. Poole, Experimental investigation of the impact of elastic turbulence on heat transfer in a serpentine channel, J. Non-Newton. Fluid Mech. **231**, 68 (2016).

[12] R. J. Poole, B. Budhiraja, A. R. Cain, and P. A. Scott, Emulsification using elastic turbulence, J. Non-Newton. Fluid Mech. **177-178**, 15 (2012).

[13] J. Mitchell, K. Lyons, A. M. Howe, and A. Clarke, Viscoelastic polymer flows and elastic turbulence in three-dimensional porous structures, Soft Matter **12**, 460 (2016).

[14] A. Fouxon and V. Lebedev, Spectra of turbulence in dilute polymer solutions, Phys. Fluids **15**, 2060 (2003).

[15] S. Berti and G. Boffetta, Elastic waves and transition to elastic turbulence in a two-dimensional viscoelastic Kolmogorov flow, Phys. Rev. E **82**, 036314 (2010).

[16] H. Garg, E. Calzavarini, G. Mompean, and S. Berti, Particle-laden two-dimensional elastic turbulence, Eur. Phys. J. E **41**, 115 (2018).

[17] A. Groisman and V. Steinberg, Elastic turbulence in curvilinear flows of polymer solutions, New J. Phys. **6**, 29 (2004).

[18] T. Burghelea, E. Segre, and V. Steinberg, Validity of the Taylor hypothesis in a random spatially smooth flow, Phys. Fluids **17**, 103101 (2005).

[19] B. Bird, C. F. Curtiss, R. C. Armstrong, and O. Hassager, *Dynamics of Polymeric Fluids* (Wiley, New York, 1987).

[20] E. Balkovsky, A. Fouxon, and V. Lebedev, Turbulence of polymer solutions, Phys. Rev. E **64**, 056301 (2001).

[21] E. L. C. VI M. Plan, A. Gupta, D. Vincenzi, and J. D. Gibbon, Lyapunov dimension of elastic turbulence, J. Fluid Mech. **822**, R4 (2017).

[22] G. Boffetta, A. Celani, A. Mazzino, A. Puliafito, and M. Vergassola, The viscoelastic Kolmogorov flow: Eddy viscosity and linear stability, J. Fluid Mech. **523**, 161 (2005).

[23] R. Sureshkumar and A. N. Beris, Effect of artificial stress diffusivity on the stability of numerical calculations and the flow dynamics of time-dependent viscoelastic flows, J. Non-Newton. Fluid Mech. **60**, 53 (1995).

[24] T. Vaithianathan and L. R. Collins, Numerical approach to simulating turbulent flow of a viscoelastic polymer solution, J. Comput. Phys. **187**, 1 (2003).

[25] M. A. Alves, P. J. Oliveira, and F. T. Pinho, Numerical methods for viscoelastic fluid flows, Annu. Rev. Fluid Mech. **53**, 509 (2021).

[26] A. Gupta and D. Vincenzi, Effect of polymer-stress diffusion in the numerical simulation of elastic turbulence, J. Fluid Mech. **870**, 405 (2019).

[27] D. O. Canossi, G. Mompean, and S. Berti, Elastic turbulence in two-dimensional cross-slot viscoelastic flows, Europhys. Lett. **129**, 24002 (2020).

[28] L. Meshalkin and Y. G. Sinai, Investigation of the stability of a stationary solution of a system of equations for the plane movement of an incompressible viscous liquid, J. Appl. Math. Mech. **25**, 1700 (1961).

[29] U. Frisch, *Turbulence. The Legacy of A. N. Kolmogorov* (Cambridge University Press, Cambridge, UK, 1995).

[30] J. O. Hinze, *Turbulence: An Introduction to Its Mechanism and Theory* (McGraw–Hill, New York, 1959).

[31] G. I. Taylor, The spectrum of turbulence, Proc. R. Soc. A **164**, 476 (1938).

[32] C. C. Lin, On Taylor's hypothesis and the acceleration terms in the Navier-Stokes equations, Q. Appl. Math. **10**, 295 (1953).

[33] J. L. Lumley, Interpretation of time spectra measured in high-intensity shear flows, Phys. Fluids **8**, 1056 (1965).

[34] W. J. A. Dahm and K. B. Southerland, Experimental assessment of Taylor's hypothesis and its applicability to dissipation estimates in turbulent flows, Phys. Fluids **9**, 2101 (1997).

[35] A. Belmonte, B. Martin, and W. I. Goldburg, Experimental study of Taylor's hypothesis in a turbulent soap film, Phys. Fluids **12**, 835 (2000).

[36] B. Ganapathisubramani, K. Lakshminarasimhan, and N. T. Clemens, Determination of complete velocity gradient tensor by using cinematographic stereoscopic PIV in a turbulent jet, Exp. Fluids **42**, 923 (2007).

[37] S. Davoust and L. Jacquin, Taylor's hypothesis convection velocities from mass conservation equation, Phys. Fluids **23**, 051701 (2011).

[38] A. Cenedese, G. P. Romano, and F. di Felice, Experimental testing of Taylor's hypothesis by L.D.A. in highly turbulent flow, Exp. Fluids **11**, 351 (1991).

[39] N. Hutchins and I. Marusic, Evidence of very long meandering features in the logarithmic region of turbulent boundary layers, J. Fluid Mech. **579**, 1 (2007).

[40] D. J. C. Dennis and T. B. Nickels, On the limitations of Taylor's hypothesis in constructing long structures in a turbulent boundary layer, J. Fluid Mech. **614**, 197 (2008).

[41] C. Geng, G. He, Y. Wang, C. Xu, A. Lozano-Durán, and J. M. Wallace, Taylor's hypothesis in turbulent channel flow considered using a transport equation analysis, Phys. Fluids **27**, 025111 (2015).

[42] S. Musacchio and G. Boffetta, Turbulent channel without boundaries: The periodic Kolmogorov flow, Phys. Rev. E **89**, 023004 (2014).

[43] E. Calzavarini, L. Jiang, and C. Sun, Anisotropic particles in two-dimensional convective turbulence, Phys. Fluids **32**, 023305 (2020).

[44] P. A. Davidson, *Turbulence: An Introduction for Scientists and Engineers* (Oxford University Press, Oxford, 2004).

[45] G. K. Batchelor, *The Theory of Homogeneous Turbulence* (Cambridge University Press, Cambridge, UK, 1953).